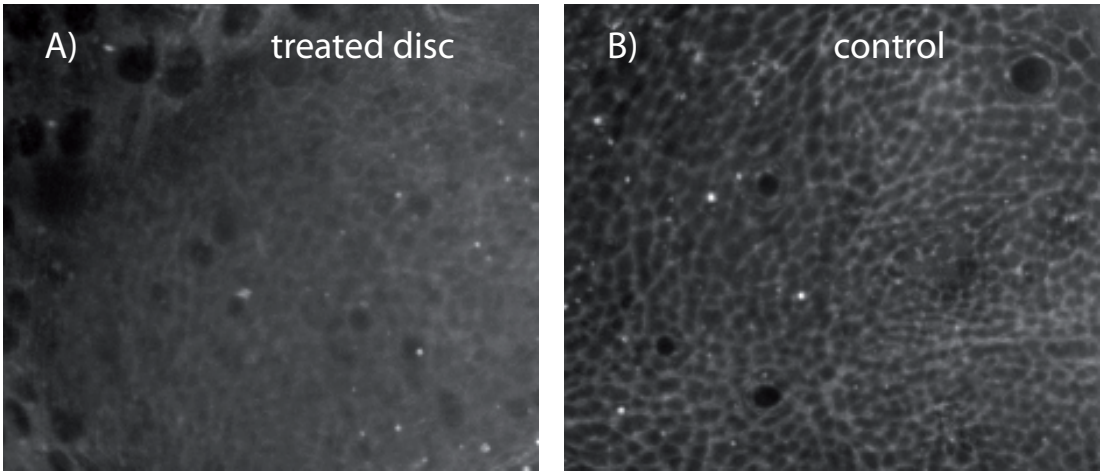

Fig. S1. Effect of Y27632 on MyoII::GFP. (**A**) A MyoII::GFP wing disc after a 40 minutes exposure to 1 mM Y27632. (**B**) The control twin disc.

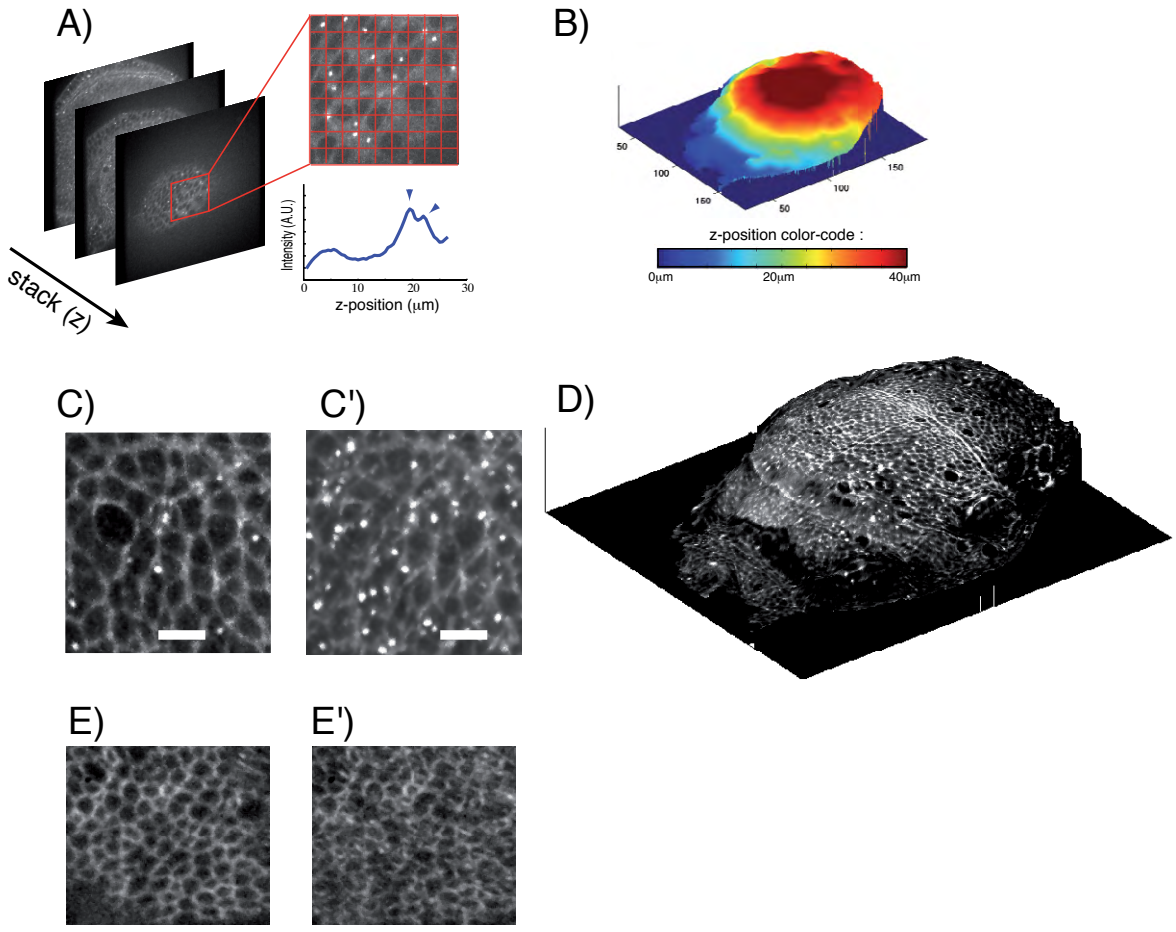

Fig. S2. Method for the selective plane projection. (**A**) After binning in *xy*, the intensity of a bin as a function of *z* shows two maxima corresponding to adherens junctions (AJs) of wing proper and peripodial cells. (**B**) 3D profile of wing-proper AJs. (**C**,**C'**) Selective plane projection (C) versus maximum intensity (C′) on MyoII-GFP. (**D**) 3D representation of the MyoII-GFP signal. (**E**,**E'**) Selective plane projection (E) versus maximum intensity (E′) on cad-GFP.

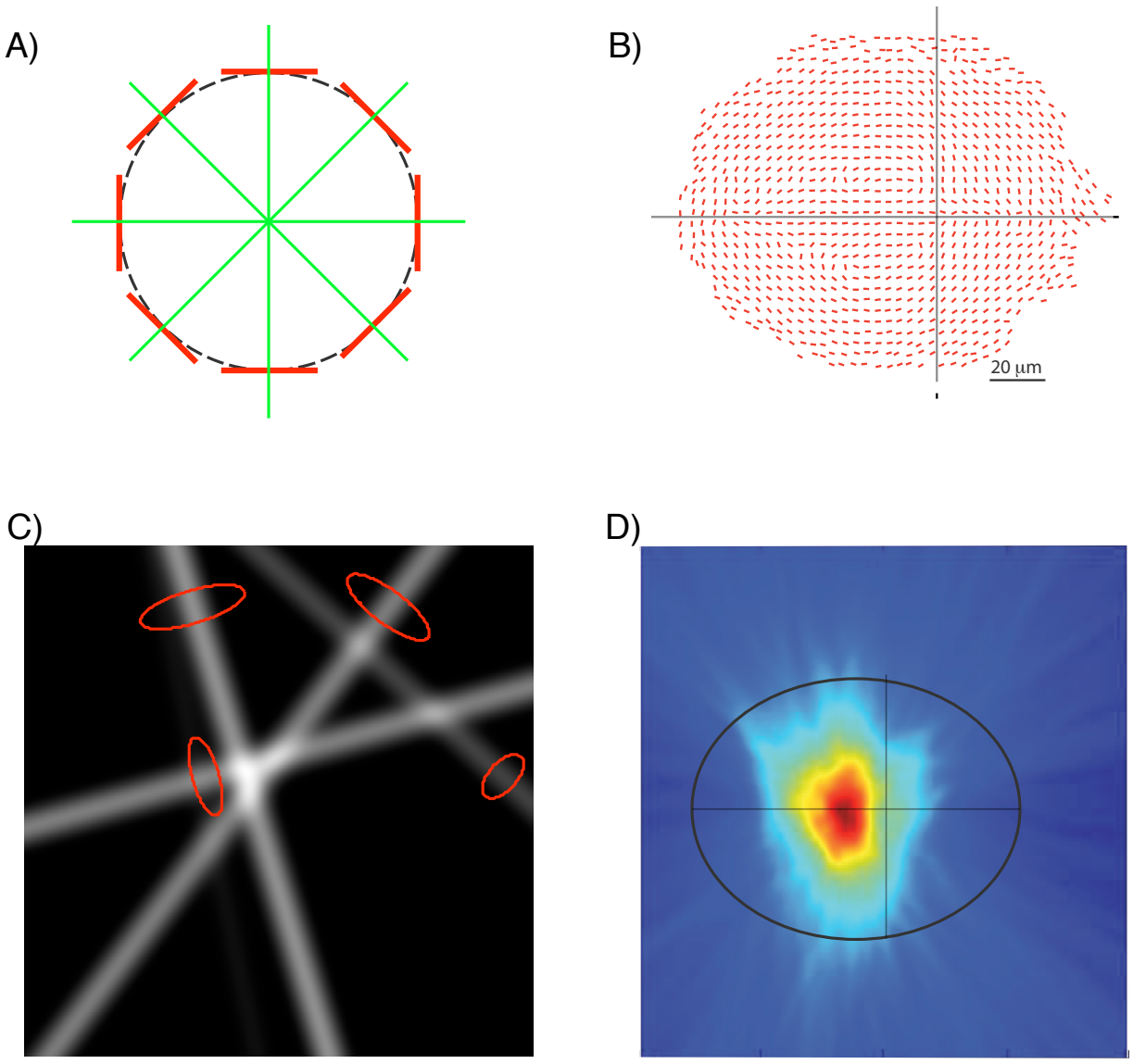

Fig. S3. Generation of the density of bisectors. (**A**) The center of a circle is found at the intersection of the bisectors (green lines) of the main axis of each cell. (**B**) The center of the pattern of orientation of the pouch can be found similarly. (**C**) The bisectors of four nearby cells. (**D**) The density of bisectors computed from the pattern of B.

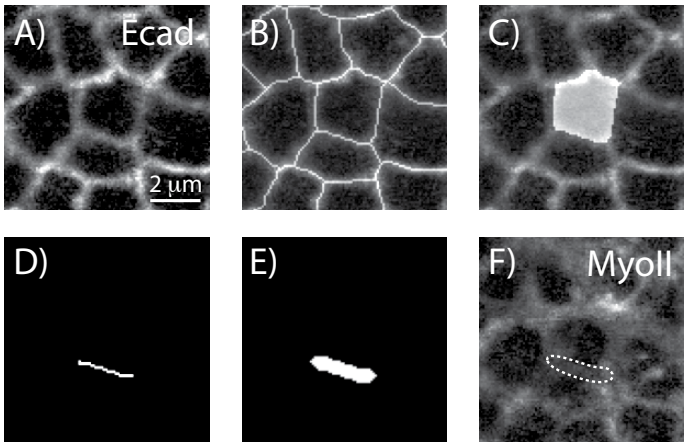

Fig. S4. Junctional enrichment analysis. (**A-C**) Ecad::GFP signal (A) overlaid with skeletonization (B) and the binary outline of one cell (C). (**D**) One cell-cell interface. (**E**) For enrichment analysis, the mask of the interface is thickened. (**F**) To measure junctional signal (here in MyoII), the average signal in the thickened junctional mask is computed.

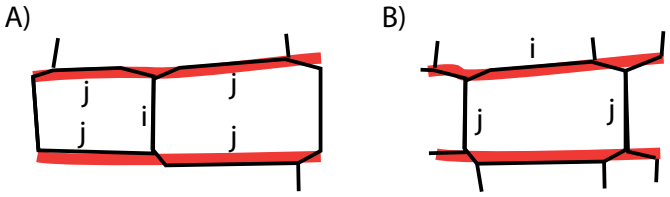

Fig. S5. Measurement of the index of polarity in MyoII cables. (**A**) Deriving the polarity index of the transverse junction i. (**B**) Deriving the polarity index of the cable junction i.

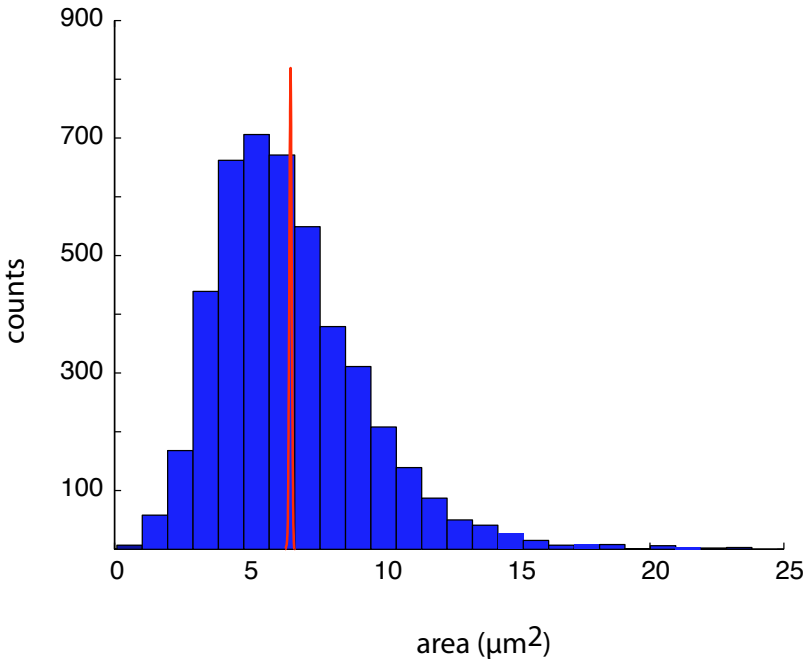

Fig. S6. Area distribution in a [34-45 μm] distance bin from the center of the pouch. The histogram shows the distribution (s.d. = 2.9 μm²). The red curve shows the distribution of 1000 bootstrapped means (s.d. = 0.042 μm2). These data correspond to the fourth point from the left in Fig. 1B′.

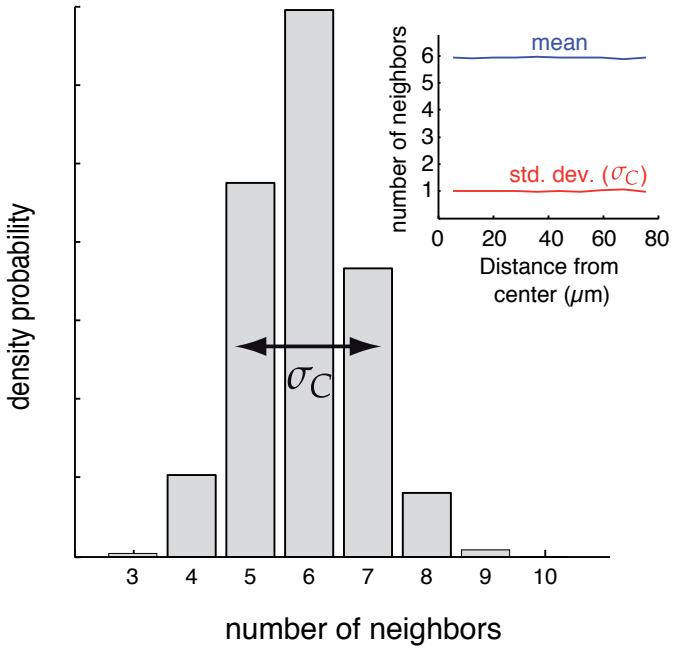

Fig. S7. Topology of cells at different locations in the tissue. The inset shows that both the mean and the width of the distribution do not significantly change as a function of the position in the tissue.

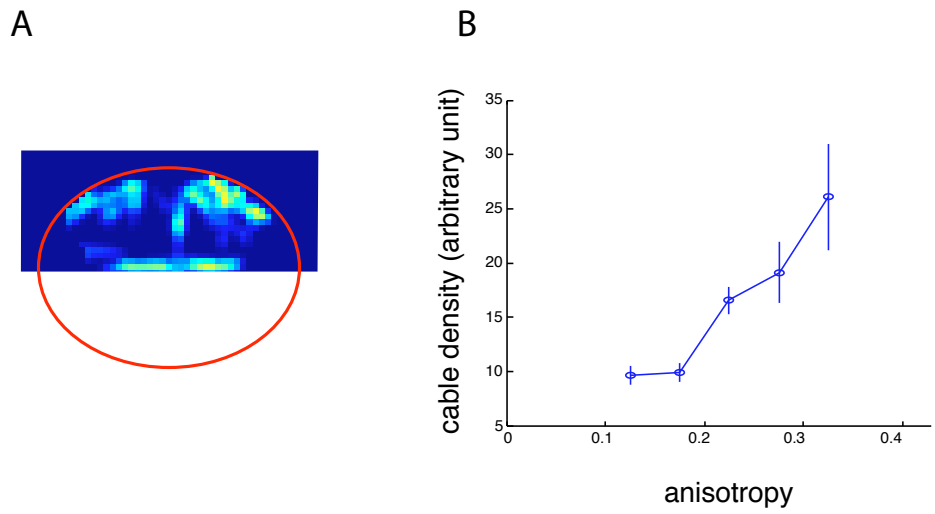

Fig. S8. MyoII cables correlate with tissue anisotropy. (**A**) The manual outline of the cables of seven pouches were register summed and low pass filtered to provide a heat map of cable density. (**B**) Anisotropy versus density of cables obtained by comparing the map of anisotropy and the map of cable density. Error bars represent s.e.m.

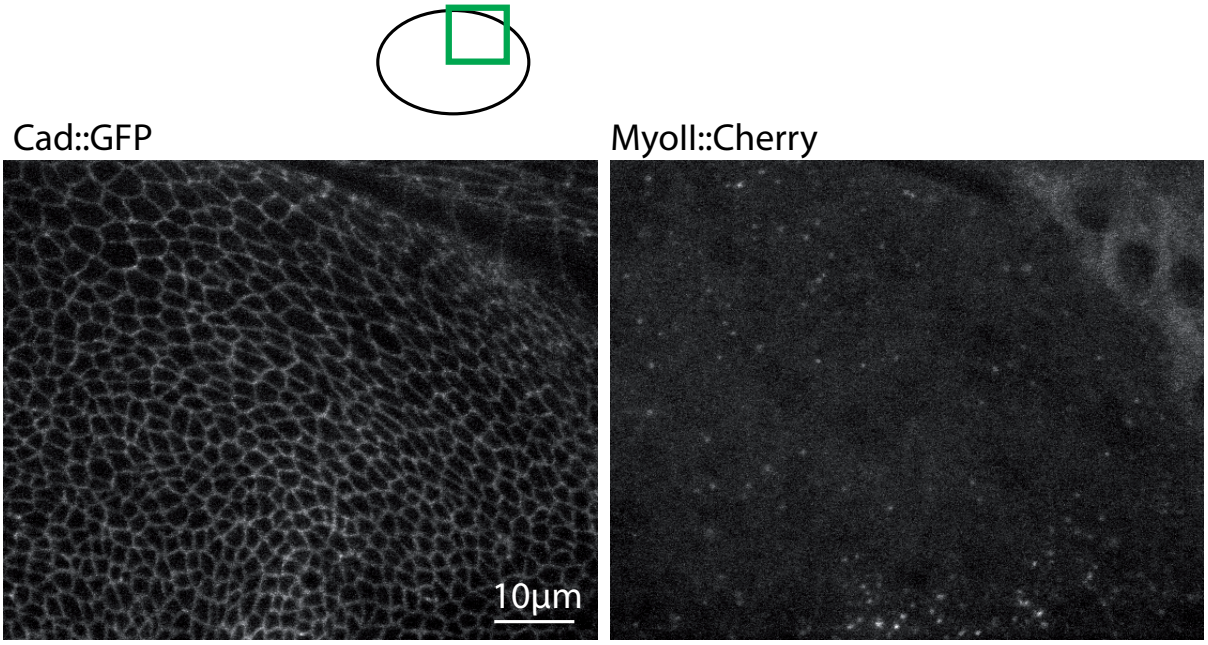

Fig. S9. Wing disc tissue after ROCK inhibitor treatment. Larger view of the disc in Fig. 5C,D, used for ablation experiments. The cartoon shows the position of the image with respect to the wing pouch. Medial cells are still smaller than peripheral ones. (**A**) Cad::GFP. (**B**) MyoII:Cherry

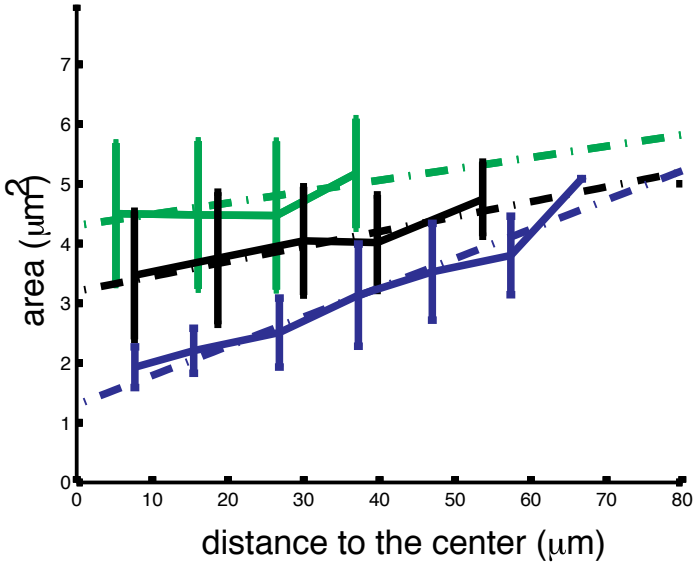

Fig. S10. Temporal evolution of the pattern of deformation. The pattern of cell area from larvae 85 hours after egg laying (AEL, green), 96 hours AEL (black), and wandering (blue) shows a gradual increase of the gradient of the cell deformation. Error bars represent s.e.m.

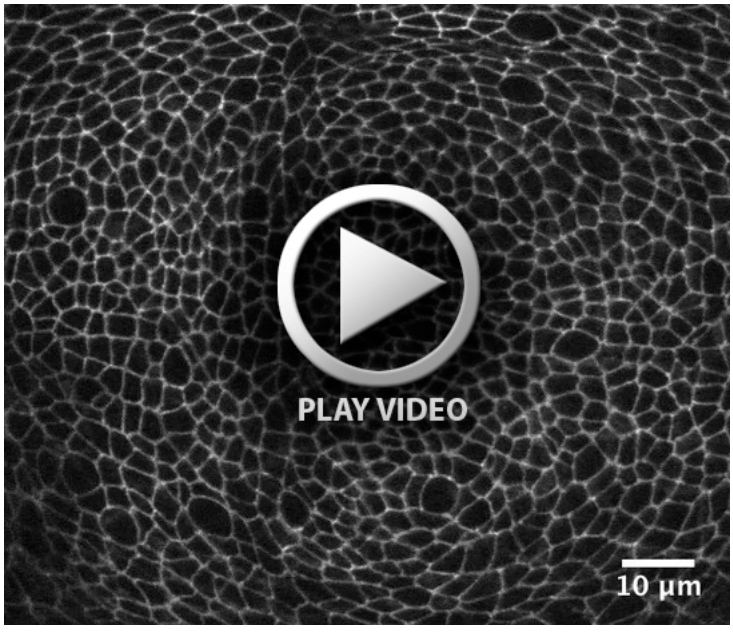

Movie 1. A time sequence of a mid-third instar wing disc imaged with a spinning disc confocal while cultured in clone 8 medium. Scale bar: 10 μm.

Movie 2 .Two examples of ablation affecting tangent junctions (red color code in Fig. 2). Scale bar: 2 µm.

Movie 3. Two examples of ablations affecting transverse junctions (blue color code in Fig. 2). Scale bar: 2 µm.

Table S1. Genotypes

	Genotype
All morphometry quantifications	*ubi-cad::GFP*
Fig. 1A	*ubi-cad::GFP*
Fig. 1C	*UAS-Gap43::Venus/+; fng-Gal4/+*
Fig. 2	*ubi-cad ::GFP*
Fig. 3B-D	*dachs-dachs::GFP*
Fig. 3E-H	*hs-flp; d^{GC13} FRT40A / ubi-GFP FRT40A*
Fig. 4A	*sqh^{AX3}; sqh-sqh::GFP; sqh-sqh::GFP*
Fig. 4B	*$sqh^{AX3;}$ubi-E-cad::GFP, sqh-sqh::mCherry*
Fig. 4C	*sqh^{AX3}; sqh-sqh::GFP ; sqh-sqh::GFP*
Fig. 4D	*dachs-dachs::GFP*
Fig. 4E	*sqh-sqh::GFP/ dachs-dachs::GFP*
Fig. 5A	*sqh^{AX3}; ubi-E-cad::GFP, sqh-sqh::mCherry*
Fig. 5B	*ubi-cad::GFP*
Fig. 5C	*sqh^{AX3}; ubi-E-cad::GFP, sqh-sqh::mCherry*
Fig. 6	*ubi-cad::GFP*
Fig. 7A-B	*$hs\text{-}flp_{122}$; ubi-cad::GFP /UAS-dcr2; AyGal4 UAS-RFP/UAS-expanded-dsRNA*
Fig. 7C	*$hs\text{-}flp_{122}$; sqh-sqh::GFP/UAS-dcr2; AyGal4 UAS-RFP /UAS-expanded-dsRNA*
Fig. 7D	*$hs\text{-}flp_{122}$; sqh-sqh::GFP / sqh-sqh::GFP; AyGal4 UAS-RFP/UAS-Yki*
Fig. 7E	*hs-flp; AyGal4 UAS-GFP/+; AyLexA LexAop-mCD8::GFP/UAS-Yki*
Fig. S1	*sqh^{AX3}; sqh-sqh::GFP; sqh-sqh::GFP*
Fig. S2A-D	*sqh^{AX3}; sqh-sqh::GFP; sqh-sqh::GFP*
Fig. S2E	*ubi-cad::GFP*
Fig. S8	*sqh^{AX3}; sqh-sqh::GFP; sqh-sqh::GFP*

Appendix S1. Image analysis

Selective plane projection

The forces that drive epithelial morphogenesis originate mainly at the level of apical junctions (AJs), which are enriched in adhesive proteins and acto-myosin cortex. We thus focus our attention on the uppermost part of epithelia, at or near AJs. The traditional approach, which consists in taking the maximum intensity projection of the stack is not optimal because it reveals bright structures that lie outside of apical junctions (such as MyoII clusters that are especially frequent in proliferating tissue due to mitotic scars), and discard dim structure of the adherens junction. This consequently reduces signal to noise ratio of the 2D projection. Furthermore, this approach ignores the 3D disposition of the 2D epithelium that might be important (*ie* curvature). We perform a selective plane projection that alleviate these issues by extracting the relevant signal exclusively from the adherens junctions, yielding a much higher signal to noise ratio. This selective plane projection (SPP) takes into account the 3D structure of the tissue.

We start from a 3D image of a wing disc. Each xy plane is then coarse grained in larger bins:

$$I_b(i,j,z) = \sum_{x=Bi}^{B(i+1)-1} \sum_{y=Bj}^{B(j+1)-1} I\,(x,y,z) \quad (1)$$

where I_b and I are the binned and unbinned image respectively, B is the bin size (equal to 20 unless otherwise specified), (i,j) and (x,y) are the positions in the binned and unbinned images respectively and z the position of the plane in the 3D stack. The inset in Fig. S2A in supplementary material shows how $I_b\ (i,j,z)$ varies with z. We distinguish two local maxima (arrowheads), which correspond to the apical junctions (which are enriched in MyoII) of the closely apposed wing disc proper and peripodial epithelium. We are interested in the former, the profile of which, $Z_{adh}(i,j)$, is then computed by local maximum finding. The coarse grained profile $Z_{adh}(i,j)$ is then refined by linear interpolation up to the original resolution of $I(x,y,z)$ (see Fig. S2B for a 3D rendering of the profile). The selective plane projection (SPP) then consists in taking the fluorescent intensity along the apical junction profile $I_{spp}(x,y) = I(x,y,Z_{adh}(i,j))$. Fig. S2C compares the same stack projected with SPP and maximum intensity. Warping $I_{spp}(x,y)$ onto the $3D$ profile of the tissue $Z_{adh}(i,j)$ generates a 3D visualization (Fig. S2D). Fine details of the tissue, such as dividing cells or actomyosin cables that span compartment boundaries, can now be apprehended in a 3D context. SPP allows the observation of cad::GFP signal in the periphery of the wing disc with much better clarity than a maximum intensity projection (Fig. S2E vs. Fig. S2E')

Skeletonization of tissues

Noise was removed from the images using a median filter. Images were then skeletonized using a crest finding algorithm (Steger, 1998). The subsequent skeleton comprised many small defects consisting of either small holes in a junction or extra segment with loose ends. The former were first corrected by applying closing morphological transformation, the latter were then corrected by applying to the binary skeleton a convolution filter of kernel $\begin{pmatrix} 1 & 1 & 1 \\ 1 & 0 & 1 \\ 1 & 1 & 1 \end{pmatrix}$, which attributes the value 1 to the ends of segment. Applying a threshold > 1 and reiterating the procedure shortens loose ends. The skeletons were eventually visually compared to the raw cad::GFP projections and manually corrected.

Texture analysis

Average orientation and anisotropy of tissue was quantified using the texture tensor introduced in (Graner et al., 2008), and defined locally for cell i by the matrix :

$$M_i = \frac{1}{N_i}\sum_{j=1}^{N_i}\begin{pmatrix} \Delta x_{ij}{}^2 & \Delta x_{ij}\Delta y_{ij} \\ \Delta x_{ij}\Delta y_{ij} & \Delta y_{ij}{}^2 \end{pmatrix} \quad (2)$$

where j stands for the successive neighbors of cell i, N_i its total number of neighbors, Δx_{ij} (resp. Δy_{ij}) is the x-coordinate (resp. y-coordinate) of the link joining the centers of mass of cell i and cell j. We performed a first order correction for the effect of tissue curvature and non flatness on texture by realizing that curvature occurs on a spatial scale much larger than the size of a cell. Thus the tissue can be considered as locally flat. A 2D texture matrix around each cell, was thus computed using the local best planar approximation. 3D positions of the center of mass of cells, a pre-requisite of the local correction, was obtained by a combination of the 2D skeleton of cells in the tissue and the 3D profile of the tissue $Z_{adh}(x,y)$, output from the selective plane projection we developed. The eigenvectors of tensor (2), $\overrightarrow{u^i_{max}}$ and $\overrightarrow{u^i_{min}}$, give the orientations of the major and minor axis of the tissue around cell i. The square root of the eigenvalues of tensor (2) give the corresponding length scale λ^i_{max} and λ^i_{min}. The local anisotropy around cell i, a_i, is then defined by :

$$a_i = \left(\frac{\lambda^i_{max} - \lambda^i_{min}}{\lambda^i_{max} + \lambda^i_{min}}\right) \quad (3)$$

Statistical morphometry

In order to remove intrinsic noise of the cellular lattice, morphometric measurements were averaged in bins of size=5-15μm within one disc, as well as averaged over 15 discs. The contour of the pouch is simply delineated by the existence of the deep folds around it, at stages posterior to 85h after egg laying. Before the presence of the folds (green in Fig.S8) the pouch can be delineated by the expression of a vestigial Qadrant enhancer reporter (Zecca & Struhl, 2007). Successive discs were registered spatially by using the antero-posterior and dorso-ventral compartment boundaries as landmarks to rotate and translate wing discs so as to superimpose them. Both compartment boundaries are clearly visible when imaging cad::GFP on living wing discs, because cell reproducibly align along these straight boundaries by a mechanism that is associated to a recruitment in MyoII (Landsberg et al., 2009; Major & Irvine, 2006). Averaging of the morphometry is simply done by computing an averaged texture tensor (2) and computing its eigenvectors and eigenvalues. The output of this statistical morphometry is a collection of maps of averaged morphometry (apical area, orientation, anisotropy). For an easier comparison with modeling, and because we find a polar symmetry in our maps (see main body of the text), these 2D maps were reduced to 1D curves by binning pixels as a function of their distance to the geometric center of the tissue (as measured from the maximum of the density of bisectors, see below) and averaging their value within each distance-bin.

Density of bisectors

In order to estimate the overlap of the pattern of local orientation (Fig. 1E) and the pattern of apical area (Fig. 1B), we transform the collection of vectors given by the map of orientation analysis into an image that encodes the probability for a pixel to be at the center of the orientation pattern of these vectors. The transformation is done by simply drawing the bisectors of all the vectors. This approach can be illustrated by considering a set of vectors that are aligned along a perfect circle (Fig. S3A in supplementary material). The center of the pattern is the center of the circle, and can be found at the intersection of the bisectors of the vectors (green line on Fig. S3A). In the more disordered case of the wing disc (Fig. S3B), bisectors do not meet at a unique point, nonetheless the zone of maximum intensity of the density of bisectors can be considered as the center of the pattern. The transformation to go from a collection of vectors to the density of bisectors is done as follows: The image of the

density of bisector is the sum of all the bisectors of the main axis of cells (as defined by the local texture) weighted by their anisotropy, and convolved with a gaussian blur to provide some spatial averaging. The intensity of this density of bisector on any point M is thus given by the formula:

$$I(M) = \sum_{k=1}^{N_{total}} \left(\frac{\lambda_{max}^k - \lambda_{min}^k}{\lambda_{max}^k + \lambda_{min}^k} \right) exp\left(- \frac{\| \overrightarrow{OM} \cdot \overrightarrow{u_{max}^k} \|^2}{\sigma^2} \right) \quad (4)$$

where N_{total} is the total number of cells analyzed, λ_{max}^k and λ_{min}^k are the characteristic distances along the major and minor axis of the k^{th} cell. O_k is the position of the k^{th} cell, and $\overrightarrow{u_{max}^k}$ is the unit vector giving the local orientation around the k^{th} cell (technically, the normalized eigen vector of the largest eigen value of the texture tensor). σ is the characteristic distance of the gaussian blur (σ=4μm). Fig. S3C shows the bisector of 4 cells, Fig. S3D show the result for all cells analyzed.

Analysis of junctional enrichment of MyoII and E-cad

The output of the skeletonization procedure is an ensemble of surfaces corresponding to the cells separated by a one pixel thick contour (Fig. S4A-C in supplementary material). Each cell is labeled, and the list of its neighbor is determined by finding those cells that overlap with it when all cells are dilated by convolution of their binary mask with the following kernel, which broadens cells by 2 pixels:

$$\begin{pmatrix} 0 & 0 & 1 & 0 & 0 \\ 0 & 1 & 1 & 1 & 0 \\ 1 & 1 & 1 & 1 & 1 \\ 0 & 1 & 1 & 1 & 0 \\ 0 & 0 & 1 & 0 & 0 \end{pmatrix} \quad (5)$$

A junction is then simply defined as the intersection of two neighbor-cells that have been dilated with the kernel 5 (Fig. S4D). The cortical enrichment of a junction (MyoII or E-Cad labeling) is subsequently measured by taking the average signal in a surface corresponding to the junction dilated with the kernel 5 (Fig. S4E-F), and subtracting the background value at the center of the cell. When required, the angle of a junction is obtained from the axis of least second moment. To assess the angular distribution of junctional enrichment, we computed the relative intensity of junctions, normalized by the mean :

$$I_i^r = \frac{I_i - \langle I \rangle}{\langle I \rangle} \quad (6)$$

where I_i^r is the relative intensity in angular bin i, I_i is the averaged intensity of junctions in angular bin i, $\langle I \rangle$ is the intensity averaged over all angular bins. To assess the angular distribution of junctional length, we computed the relative length of junctions, normalized by the mean :

$$L_i^r = \frac{L_i - \langle L \rangle}{\langle L \rangle} \quad (7)$$

where L_i^r is the relative summed length in angular bin i, L_i is the sum of the length of all junctions in the angular bin i, $\langle L \rangle$ is the summed length averaged over the angular bins.

The index of polarity used to analyze ablation experiments in MyoII cables and their transverse dim counterparts was computed with

$$P^i = \frac{I_{junct}^i - < I_{junct}^j >_j}{< I_{junct}^j >_j} \quad (8)$$

where $<>_j$ denotes the average over j, the neighboring junctions of the junction i analyzed as depicted on Fig. S5A-B